Angular momentum evolution in dark-matter haloes

Laura G. Book,[1]★ Alyson Brooks,[1] Annika H. G. Peter,[1] Andrew J. Benson[1]
and Fabio Governato[2]

[1]*Mail Code 350-17, California Institute of Technology, Pasadena, CA 91125, USA*
[2]*Astronomy Department, University of Washington, Box 351580, Seattle, WA 98195, USA*

ABSTRACT

We have analysed high-resolution *N*-body simulations of dark-matter (DM) haloes, focusing specifically on the evolution of angular momentum. We find that not only is individual particle angular momentum not conserved, but the angular momentum of radial shells also varies over the age of the Universe by up to factors of a few. We find that torques from external structure are the most likely cause for this distribution shift. Since the model of adiabatic contraction that is often applied to model the effects of galaxy evolution on the DM density profile in a halo assumes angular momentum conservation, this variation implies that there is a fundamental limit on the possible accuracy of the adiabatic contraction model in modelling the response of DM haloes to the growth of galaxies.

Key words: galaxies: haloes – galaxies: kinematics and dynamics.

1 INTRODUCTION

Recent years have seen much progress in our understanding of the growth of dark-matter haloes from initial density fluctuations and the characterization of their properties. For example, it has been possible to find analytic results to describe the merger trees of dark-matter-only systems (Press & Schechter 1974; Sheth & Tormen 2002; Benson, Kamionkowski & Hassani 2005; Neistein & Dekel 2008; Parkinson, Cole & Helly 2008; Zhang, Fakhouri & Ma 2008). Additionally, high-resolution *N*-body simulations containing only cold (i.e. non-relativistic at the epoch of kinetic decoupling) dark matter have been performed (Springel et al. 2005; Kuhlen et al. 2008; Boylan-Kolchin et al. 2009; Stadel et al. 2009; Klypin, Trujillo-Gomez & Primack 2010), leading to detailed knowledge of the structure of cold dark-matter haloes, such as the fact that haloes have an approximately universal radial density profile (Navarro, Frenk & White 1997; Navarro et al. 2004, 2010) and are generally triaxial in shape (Dubinski & Carlberg 1991).

There is currently a great deal of interest in the angular momentum of particles in dark-matter haloes, since it is this angular momentum, when transferred to baryons, that creates the discs of galaxies. It is also interesting to look at this topic in the light of the adiabatic contraction (AC) model, which is used to model how the condensation of baryons during the formation of a galaxy affects the mass profile of its host halo (e.g. Mo, Mao & White 1998; Cole et al. 2000; Somerville et al. 2008; Benson & Bower 2010). In this model, it is assumed that the gravitational potential of the system changes very slowly, so that it can be ap-

proximated as adiabatic. Further, two simplifying assumptions are usually employed to calculate the density increase resulting from the growth of galaxies at centres of dark-matter haloes using AC. First, the gravitational potential of the system (including contributions from both the dark-matter halo and the galaxy) is assumed to be spherically symmetric and the orbits of particles are presumed to be circular, such that the angular momentum of particles is conserved.

The backreaction of the evolution of those galaxies on the dark matter is poorly understood. The properties of the galaxy population and of the dark-matter response appear to depend quite strongly on the star formation prescription and strength of feedback processes, among other things, but a physically motivated and vetted mapping between baryonic physics and the evolution in the dark-matter phase-space density is lacking (Cole et al. 2000; Gnedin et al. 2004; Gustafsson, Fairbairn & Sommer-Larsen 2006; Romano-Díaz et al. 2008, 2009; Somerville et al. 2008; Abadi et al. 2009; Tissera et al. 2010; Benson & Bower 2010; Duffy et al. 2010; Governato et al. 2010).

The development of an accurate model of this backreaction is required to accurately compare theoretical predictions of galaxy formation, in the context of both canonical cold-dark-matter and alternative dark-matter cosmologies with observations. A number of observed galaxy properties, such as the rotation curves of disc galaxies and the associated Tully–Fisher relation (Tully & Fisher 1977), depend on the gravitational potential of both baryons and dark matter. In particular, the Tully–Fisher relation is frequently used as a constraint on galaxy-evolution processes in models of galaxy formation (Cole et al. 2000; Hatton et al. 2003; De Lucia, Kauffmann & White 2004; Croton et al. 2006; Dutton et al. 2007; Monaco, Fontanot & Taffoni 2007; Somerville et al. 2008; Dutton

★E-mail: lbook@caltech.edu

& van den Bosch 2009; Benson & Bower 2010). Moreover, different dark-matter candidates are expected to have noticeably different distributions in dark-matter haloes in the absence of baryons (e.g. Spergel & Steinhardt 2000; Abazajian, Fuller & Patel 2001; Feng, Rajaraman & Takayama 2003; Kaplinghat 2005); it is not clear how these distributions will change as a result of baryonic physics. Observed density profiles sometimes appear consistent with cold-dark-matter predictions in the absence of baryons and sometimes do not (Padmanabhan et al. 2004; Treu & Koopmans 2004; Simon et al. 2005; Gavazzi et al. 2007; de Blok et al. 2008; Kuzio de Naray, McGaugh & de Blok 2008; Newman et al. 2009; Schulz, Mandelbaum & Padmanabhan 2010).

In the absence of a physically vetted predictive model for the impact on baryonic physics processes on dark-matter distributions in haloes, variations on the AC model are often applied to compare galaxy evolution and dark-matter theories with observations (e.g. Mo et al. 1998; Cole et al. 2000; Somerville et al. 2008; Benson & Bower 2010). In its most general form, AC applies if the halo potential is only slowly evolving and is integrable, such that the Hamiltonian and the distribution function (DF) of particles are fully described by action variables. If the time-scale for changes in the potential is long compared to the typical dynamical time of particles in the halo, the action variables are invariant under changes in the potential and the DF (when expressed in those action variables) is therefore also invariant with time (Binney & Tremaine 2008). However, transforming from a DF to a spatial distribution is non-trivial, and so simple approximations to the true AC model are often used instead. The two most common simplifying assumptions are that the gravitational potential (from both the dark matter and the galaxy) is spherically symmetric, such that the magnitude of the angular momentum and the radial action are the relevant action variables, and that all orbits are circular such that angular momentum is the only non-zero and non-infinite-period angle variable (Blumenthal et al. 1986). Occasionally, the assumption of circular orbits is swapped in favour of choosing a variant of the radial action as a conserved quantity (Blumenthal et al. 1986; Gnedin et al. 2004). One can thus analytically calculate the final mass profile of the dark matter given the growth of the galaxy. Although these simple models have a mixed track record of matching observations and hydrodynamic simulations of galaxy evolution, they are currently the only predictive models for the effects of galaxy evolution on the dark-matter profile in haloes (Treu & Koopmans 2004; Simon et al. 2005; Gustafsson et al. 2006; Gavazzi et al. 2007; de Blok et al. 2008; Kuzio de Naray et al. 2008; Romano-Díaz et al. 2008, 2009; Abadi et al. 2009; Dutton & van den Bosch 2009; Schulz et al. 2010; Tissera et al. 2010; Duffy et al. 2010; Governato et al. 2010).

In this work, we examine two key assumptions of the AC model in the context of dark-matter-only simulations of galaxy-mass haloes: the adiabaticity of the evolution of the gravitational potential and the angular momentum distribution of dark-matter particle haloes. Specifically, we will investigate the extent to which angular momentum is invariant for individual particles and subsets of particles, as is assumed in the spherically symmetric model that is generally applied (and which will be true even if particle orbits are non-circular). Invariance may be broken for a number of reasons, including a breakdown of the adiabatic assumption, the non-sphericity of the halo potential and torques from the external mass distribution. Even if the angular momentum of individual particles is not conserved due to the triaxiality of the halo density profile, AC might be applicable if the *distribution* of angular momenta of all particles were invariant with time. If the angular momentum distri-

bution varies with time, then the simple model of AC cannot work precisely for even the simplest galaxy-evolution models.

Note that, as we are working with dark-matter-only simulations, we set only lower limits on the level to which AC is not applicable in haloes with both dark matter and baryons, as the inclusion of baryonic physics is likely to exacerbate these effects. The observed angular momentum distribution of baryons in galaxies has been shown to deviate significantly from that expected based on simulations (van den Bosch, Burkert & Swaters 2001; van den Bosch et al. 2002; van den Bosch, Abel & Hernquist 2003), so we do not expect the angular momentum distribution that we measure to be representative of the baryonic distribution of angular momenta. However, the extent of non-conservation of angular momentum in dark-matter-only simulations is likely to be less than that when baryons are added, since baryons and dark matter can exchange angular momentum. Hence, in this paper, we examine the accuracy of the adiabatic assumption and the level to which the angular momentum distribution changes with time in dark-matter-only simulations, as this places a limit on the possible accuracy of the AC model. Our intention is not to provide a precise quantification of this limit, but merely to highlight its existence and provide an approximate measure of its magnitude.

This paper is organized as follows. In Section 2 we describe the simulations and haloes that we analyse, and in Section 2.1 we describe the particle subsets that we use in the paper. We show how the average angular momentum of halo particles with respect to the centre of mass is evolving in Section 3, and analyse the extent to which the adiabatic approximation is valid in the haloes in Section 3.1. In Section 3.2, we present the evolution of the average angular momentum of halo particles with respect to the centre of the halo, and in Section 3.3 we present the evolution of the angular momentum distribution. Finally, we examine the causes of this evolution in Section 4 and discuss our results in Section 5.

2 SIMULATIONS

The dark-matter haloes used in this study were simulated with the code PKDGRAV (Stadel 2001) using a *Wilkinson Microwave Anisotropy Probe* 3-yr cosmology ($\Omega_m = 0.24$, $\Omega_\Lambda = 0.76$, $H_0 = 73$ km s^{-1}, $\sigma_8 = 0.77$; Spergel et al. 2007). These four haloes were originally chosen from a low-resolution volume of 50 Mpc on a side and selected to span a range of merger histories and spin values at roughly the mass of the Milky Way halo. Each halo was then resimulated using the volume renormalization technique (Katz & White 1993). This approach creates successively finer resolution layers around the halo of interest, allowing for high resolution on one halo while maintaining the large-scale structure (from the original 50-Mpc box) at lower resolution. Importantly, the large-scale structure can deliver tidal torques and angular momentum to the halo.

Table 1 lists properties of each of the simulated haloes. Three of the four haloes have been presented at similar resolution, but including gas through smoothed particle hydrodynamics, in previous papers (e.g. Brooks et al. 2009; Governato et al. 2009; Read et al. 2009; Zolotov et al. 2009; Pontzen et al. 2010). As examined in Read et al. (2009) and Governato et al. (2009), halo h258 has an approximately binary merger that occurs at $z \sim 1$ but exhibits a very quiescent evolution afterwards. Zolotov et al. (2009) showed that h277 has a fairly quiescent merger history back to $z \sim 3$, while h285 experiences a large number of minor mergers all the way to redshift 0, despite not having a major merger since high redshift.

Table 1. Simulated galaxy properties.

Simulation	M_{vir} ($M_\odot$)	λ^a	z_{LMM} [b]	N within R_{vir} [c]
H239	9.3×10^{11}	0.01	1.25	7.6×10^5
H258	8.2×10^{11}	0.03	1.25	6.7×10^5
H277	7.2×10^{11}	0.03	2.5	5.9×10^5
H285	7.4×10^{11}	0.02	3.75	6.1×10^5

[a]Global spin parameter as defined in Bullock et al. (2001).
[b]Redshift of the last major merger.
[c]Number of dark-matter particles within the virial radius at $z = 0$.

Halo h239 is presented here for the first time. It has a continually active merger history, both major and minor, until $z \sim 0.5$.

The mass resolution of the particles that make up these haloes is 1.2×10^6 $M_\odot$, with a spline force softening of 350 pc. At each output time-step (~ 80 Myr), high-resolution haloes with more than 64 particles (above which the mass function converges, Reed et al. 2003; Governato et al. 2007) in the volume are identified using AMIGA's Halo Finder (AHF, Gill, Knebe & Gibson 2004; Knollmann & Knebe 2009). AHF adopts results from Gross (1997), calculating the overdensity assuming a spherical top hot collapse, under the assumption that the halo has just virialized. The definition for δ_{vir} differs from its value as defined in Eke, Cole & Frenk (1996) by the factor $\Omega(z) \times (1 + \delta_{vir})$. Thus Δ_c, the value for which $\rho_{vir} = \Delta_c \rho_{crit}$, is ~ 100 at $z = 0$. We follow the main halo through time by identifying the most massive progenitor at high redshift.

2.1 Particle subsets

There are several different subsets of particles whose properties we analyse here. We take two different approaches to selecting particles; in the first case, we choose particles based on their radius relative to the halo centre at $z = 0$ and follow these same particles back through the simulation (Lagrangian selection), while in the second case we choose particles based on their radius at each time-step (Eulerian selection). We use the Lagrangian method to highlight the evolution over the course of the simulation of those particles that will be at a certain radius at $z = 0$. The Eulerian approach is complementary, as it shows how the particles at a certain radius at each time-step are related. This is relevant in the context of galaxy evolution, as the baryons condense to a specific region of physical space.

We also use two different methods of averaging the angular momenta of particles, one adding them as vectors and the second simply adding their magnitudes. These methods also highlight different features of the angular momentum distribution. The vector addition of angular momenta allows us to see the extent to which a given set of particles have their angular momenta aligned, as a decrease in angular momentum may represent a mixing of angular momentum directions as well as a change in magnitude. Thus, the vector-averaged angular momentum of a radial shell of particles is essentially telling us about the evolution of the 'spin' of that shell. In contrast, adding the magnitudes allows us to single out only the change in the magnitude of particle angular momentum and therefore tells us about changes in the particle orbits. It is this quantity which is relevant for the DF and adiabatic invariance.

3 HALO EVOLUTION

Before we describe the evolution of the angular momentum distribution in the simulations outlined in Section 2, we show the results

of two simple checks. First, to determine that any evolution in the angular momentum distribution is real and not a numerical artefact, we simulated a 10^{12}-$M_\odot$, spherically symmetric halo with equilibrium initial conditions, which in the absence of a spurious numerical effect would maintain a static distribution of angular momenta. These initial conditions were used in Peter, Moody & Kamionkowski (2010) in the context of decaying dark matter.[1] The orbits of 10^6-$M_\odot$ particles were integrated for 10 Gyr using PKDGRAV (Stadel 2001). We found no secular drift in the angular momentum distribution of particles in the halo, just as we expected for a spherically symmetric halo in equilibrium. Further, we found that the angular momentum distribution in radial shells is invariant with time. Thus, we determined that the angular momentum evolution that we see in the cosmological case is not due to numerical effects.

As a further check, we compared the evolution of the total centre-of-mass angular momentum of our cosmological models with that found by other authors. In Fig. 1, we plot the specific halo angular momentum *with respect to the centre of mass of the system* of all particles that are within the virial radius of the halo at $z = 0$ (i.e. the Lagrangian region corresponding to the $z = 0$ halo) for haloes (a) 239, (b) 258, (c) 277 and (d) 285, as a function of the cosmological scalefactor a. Specifically, in the top panel of each panel we show the specific angular momentum L, as defined above in the centre-of-mass frame, divided by its value L_0 at $z = 0$. Tidal torque theory, as was first calculated by White (1984) and was observed in simulations by Zavala, Okamoto & Frenk (2008), implies that the specific angular momentum of a halo grows as $a^{3/2}$ until the halo virializes, at which point it becomes roughly constant. In the bottom panels, we show the L/L_0 now divided by $a^{3/2}$ to explicitly remove this expected dependence. We find that in most of our haloes, the angular momentum defined with respect to the centre of mass of the system behaves in the manner expected from tidal torque theory. Halo 239 also follows this trend but has significantly bumpier evolution than the other haloes, possibly as a result of its continuously active merger history.

3.1 Validity of the adiabatic approximation

To determine how well the prescription of AC is followed in simulations, we must first determine to what extent the potential of a halo evolves adiabatically. The AC model is only applicable if the typical time-scale for order unity changes to the halo gravitational potential is long compared to the dynamical time of a typical particle in the halo. If this is not the case, it would be an indication that the AC approximation may not be used.[2]

To answer this question, we examined the energies and time-scales of all particles within the virial radius of each halo. We show these quantities for halo 239 in Figs 2 and 3. The top panel in Fig. 2 shows the dynamical time of the entire halo, defined as the virial radius divided by the virial velocity, with the time-scale for the potential of the entire halo to change by order unity. The potential change time-scale is defined as $t_{pot} = |\Phi/(d\Phi/dt)|$ and has been smoothed on the dynamical time of the halo. It can be seen that, in general, the dynamical time is at least an order of magnitude smaller than the time-scale for the gravitational potential to change by order unity, implying that the adiabatic approximation is reasonably accurate in these regions. However, when a halo experiences

---

[1] No decay term was included in this work, however.
[2] This does not, of course, address the issue of whether changes in the potential remain adiabatic once baryonic physics are included.
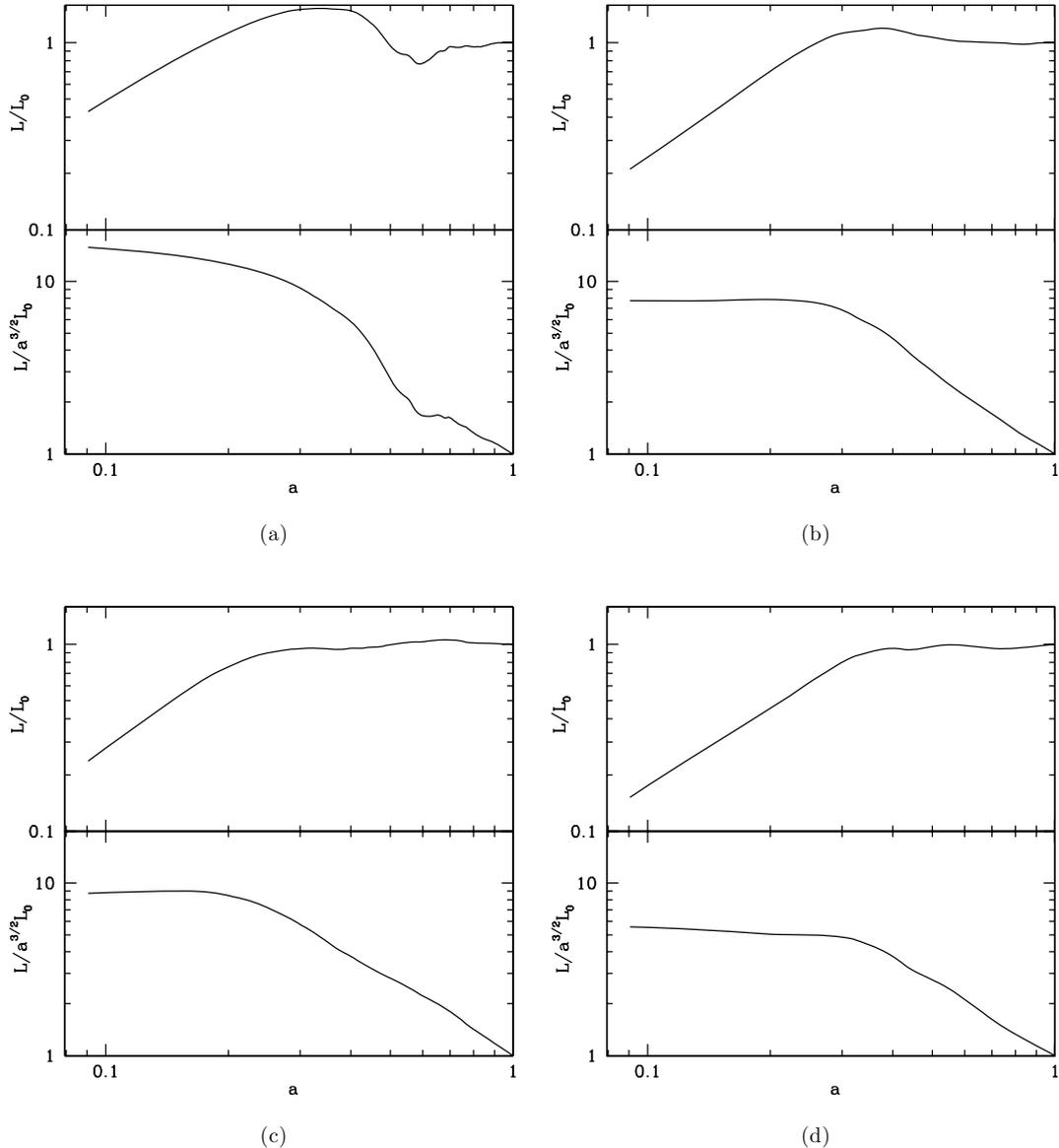
Figure 1. The evolution of the specific halo angular momentum, with respect to the centre of mass of the system, of all particles that are within the virial radius of the halo at $z = 0$ for haloes (a) 239, (b) 258, (c) 277 and (d) 285. All haloes follow a basic trend that agrees with the results of tidal torque theory (White 1984; Zavala et al. 2008).

a merger, the potential change time-scale is reduced and the evolution of the potential is non-adiabatic. Such mergers occur here at redshifts 2.2 and 1.2, with mass ratios of 1.1 and 1.9, respectively. The bottom panel of Fig. 2 shows the evolution of the potential and kinetic energy of all particles within the virial radius at each time-step and shows that the halo reaches a stable quasi-equilibrium around a redshift of $z = 1$. Overall, we see that the halo is roughly adiabatically evolving, particularly after this redshift.

As galaxies generally form in the inner regions of their host haloes, we would also like to determine whether the adiabatic approximation is valid in the innermost regions of haloes. This can be seen in Fig. 3, which shows the same quantities as Fig. 2 but for only those halo particles that are within the Eulerian-selected region $r(z) < 0.1 r_{vir}(z = 0)$. The potential change time-scale of the inner halo is generally much closer to the dynamical time of this region, implying that the adiabatic approximation is less valid for the inner halo. We can see from the evolution of the kinetic and potential ener-

gies that the inner region reaches a state of stable quasi-equilibrium around $z = 1$, similar to the outer regions. However, we note that halo 239 has a more rapid change in angular momentum than the other haloes (see Fig. 1). Thus, we would expect the other haloes to have larger angular momentum change time-scales and the adiabatic approximation to be more correct in those cases.

These figures show that the approximation that the halo is evolving adiabatically is roughly accurate for the haloes studied herein, although the dynamical time is often only an order of magnitude or less smaller than the potential change time-scale. The entire halo reaches a quasi-equilibrium by around $z = 1$ here, while haloes with more quiescent merger histories reach an equilibrium earlier. However, in the inner regions of the halo where a galaxy might form, the adiabatic approximation is not as good, with the potential time-scale usually above but frequently close to the dynamical time-scale. Thus, we must apply the assumption of adiabaticity with caution to the inner regions of the halo, and to some extent even
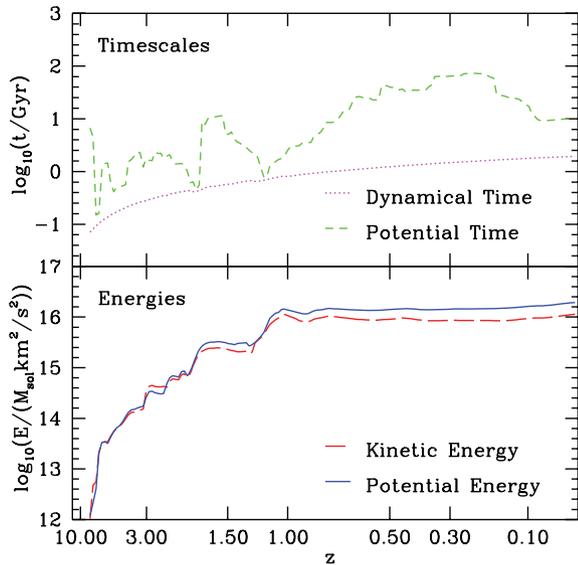
Figure 2. Energies and time-scales of all particles within the virial radius at each time-step. The halo shown is halo 239. The top panel shows the dynamical time of the entire halo versus the time-scale for changes to the gravitational potential, which has been smoothed over the dynamical time of the halo. The bottom panel shows the evolution of the potential and kinetic energy of all particles within the virial radius at each time-step.
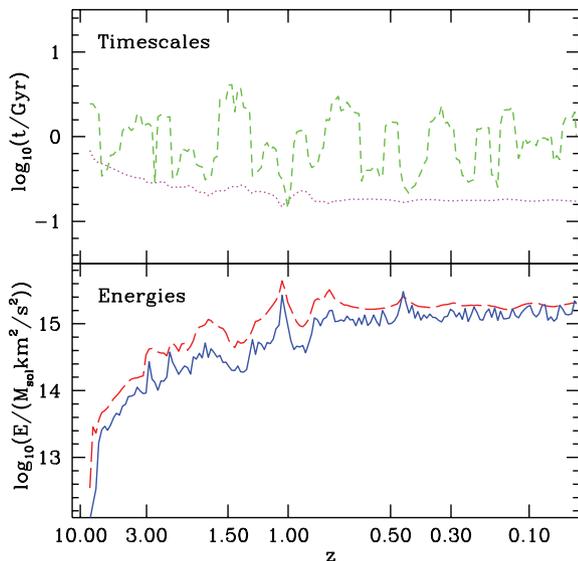
Figure 3. The same quantities as Fig. 2, but for only those halo particles that are at each time-step within a physical radius $0.1r_{\rm vir}(z=0)$ of the centre of the halo.

to the outer regions, especially as work in the context of decaying dark matter has shown that AC works well only if the time-scale for changes in the potential is much longer than the dynamical time (Peter et al. 2010).

3.2 Angular momentum evolution

We next examine the extent to which angular momentum is conserved in our dark-matter-only haloes. Here, we consider only angular momentum with respect to the centre of the halo, and not the centre of mass [as in e.g. the comparison with Zavala et al. (2008) at

the beginning of this section]. The centre of the halo is determined by AHF, which uses an adaptive mesh to search for overdensities in the simulation. Once it identifies a halo, it defines the centre of the halo as the centre of mass of the particles on the highest refinement grid. We show the average particle angular momentum as it evolves over the course of the simulation for various groups of particles, chosen to emphasize particular physical characteristics of the system. In all cases, we bin particles radially so that the innermost 10 per cent of the halo particles are placed into bin 0, the next 10 per cent into bin 1 and so forth.

We present this information in Figs 4 and 5. In Fig. 4, we show the evolution of the vector-averaged angular momentum of particles chosen to lie within radial bins interior to the virial radius at $z = 0$ (Lagrangian radial selection, black solid lines), compared to the evolution of the vector-averaged angular momentum of all particles within the virial radius at $z = 0$ (blue dashed lines), for haloes (a) 239, (b) 258, (c) 277 and (d) 285. The angular momenta in these plots were vector-added and then divided by the particle number to obtain the average, i.e. the specific angular momentum. Particles were placed into 10 radial bins at $z = 0$, and we show the 0th (innermost with respect to the halo centre), 5th (middle) and 9th (outermost) bins in the top, middle and bottom panels of each plot, respectively. We also show the redshift at which the average radius of particles in this radial bin passes within the virial radius of the halo (green dot–dashed vertical lines), and the ratios of the angular momentum at $z = 1$ and at the redshift of their accretion on to the halo to illustrate quantitatively the extent of angular momentum loss. In this plot, we can see that generally, the particles that end up in the inner regions of these haloes at $z = 0$ lose a larger fraction of their angular momentum than those that end up in the outer regions, and the angular momentum of these $z = 0$ inner particles also fluctuates more rapidly. The blue dashed line, which shows the evolution of the average angular momentum of all particles within the virial radius at $z = 0$, shows the average behaviour of the particles in all bins and, like the binned behaviour, always decreases.

As mentioned earlier, the angular momentum of particles selected based on their Eulerian radius is an interesting complement to the Lagrangian case as it shows how those particles that are in a given radial bin at each time-step evolve in angular momentum, and thus more clearly illustrates the evolution of the radial angular momentum profile of the halo. By contrast, the angular momentum evolution of radially Lagrangian-selected particles shows how the angular momentum of those particles which end up in certain radial bins have changed over time.

The quantities shown in Fig. 5 are similar to those in Fig. 4, except that the particles here (specifically, all particles that are within the virial radius at $z = 0$) were binned radially at each time-step in a Eulerian fashion, so that the 'bin 0' line shows the specific angular momentum of the 10 per cent of particles that are closest to the centre of the halo at each time-step. The magenta long-dashed line shows the specific angular momentum of all particles that are within the virial radius at each time-step. This quantity goes to zero at the beginning of the simulation as the virial radius is zero at the first time-step and increases from there. This line tends to increase because the virial radius increases with time. This is different from the binned values which include all particles that are within the virial radius at $z = 0$ and thus always contain a non-zero number of particles. All of the angular momenta in this plot were vector added as in the previous figure.

In Fig. 5, there is no clear pattern as to which bin loses a larger fraction of its angular momentum, although the inner bin generally has less angular momentum. This shows that, in general, particles
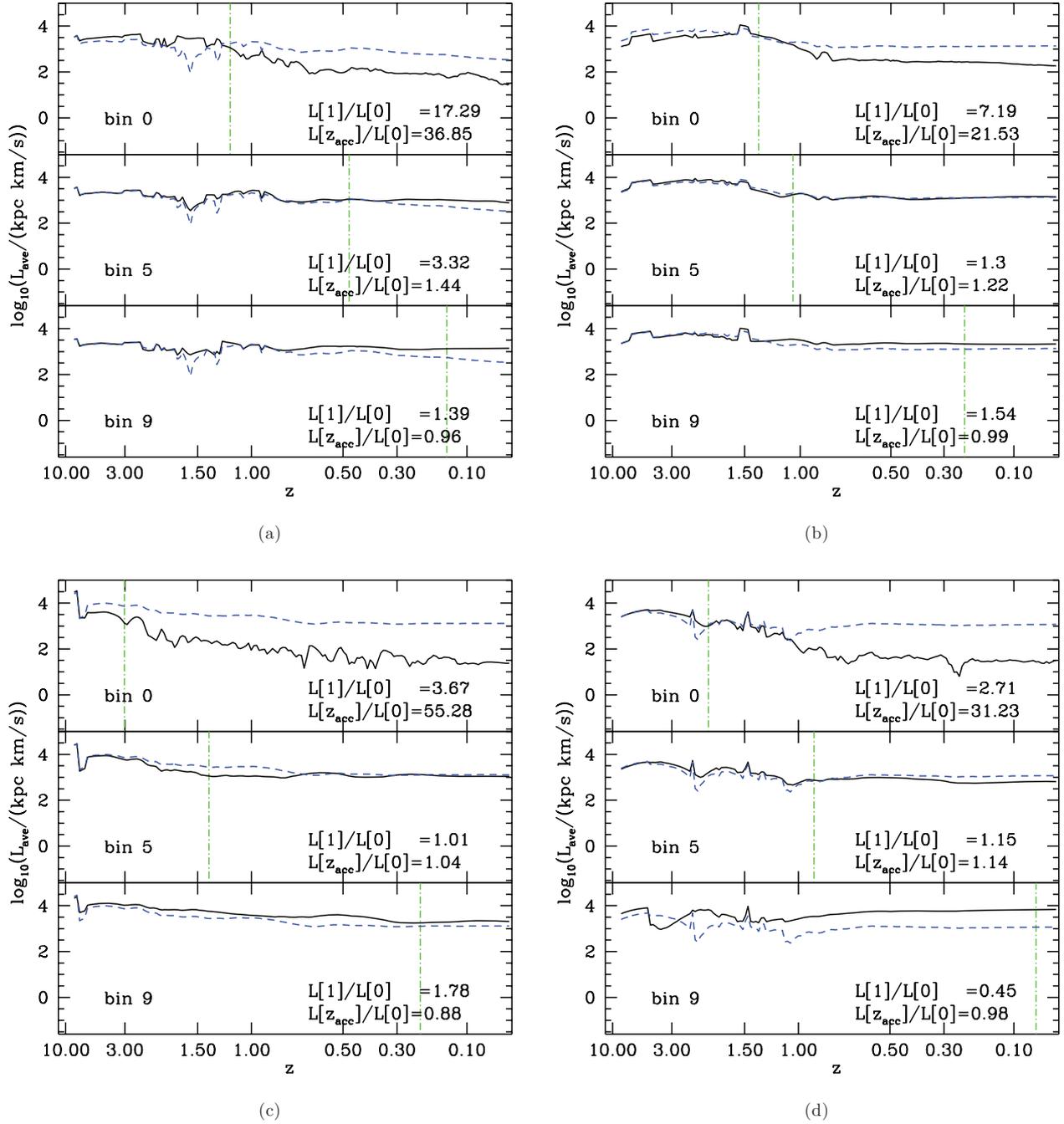
Figure 4. The evolution of the average angular momentum of particles chosen in a Lagrangian fashion to lie within the 0th, 5th and 9th of 10 radial bins (black solid lines) compared to the evolution of the average angular momentum of all halo particles that are within the virial radius at $z = 0$ (blue dashed lines), for haloes (a) 239, (b) 258, (c) 277 and (d) 285. The angular momenta in these plots were vector-averaged, and we show the redshift at which each bin is accreted on to the halo (green dot–dashed vertical lines). In each panel is given the ratios of the angular momentum at $z = 1$ and at the redshift of their accretion, z_{acc}, on to the halo to the value at $z = 0$.

throughout the halo lose a comparable fraction of their angular momentum, but those in the inner regions at each time-step tend to have less angular momentum than those in the outer regions. However, we saw in Fig. 4 that when the particles were binned in a Lagrangian fashion, the particles in the inner regions lost a larger fraction of their angular momentum as well as having in general lower angular momentum. Noting that both Figs 4 and 5 must and do converge to the same value at $z = 0$, this implies that the particles that end up in the innermost bin at $z = 0$ both begin with a larger

angular momentum than those particles that are in the innermost bin at the beginning of the simulation and subsequently lose this angular momentum at a faster rate than those particles that are at each time-step at the centre of the halo. This behaviour is to be expected, as the particles at the centre of the halo at each time-step will tend to have a low angular momentum, and it is reasonable to expect that this value will tend to drop rather slowly since we are choosing new, low-angular-momentum sets of particles at each time-step in the innermost bin.

(a)

(b)

(c)

(d)
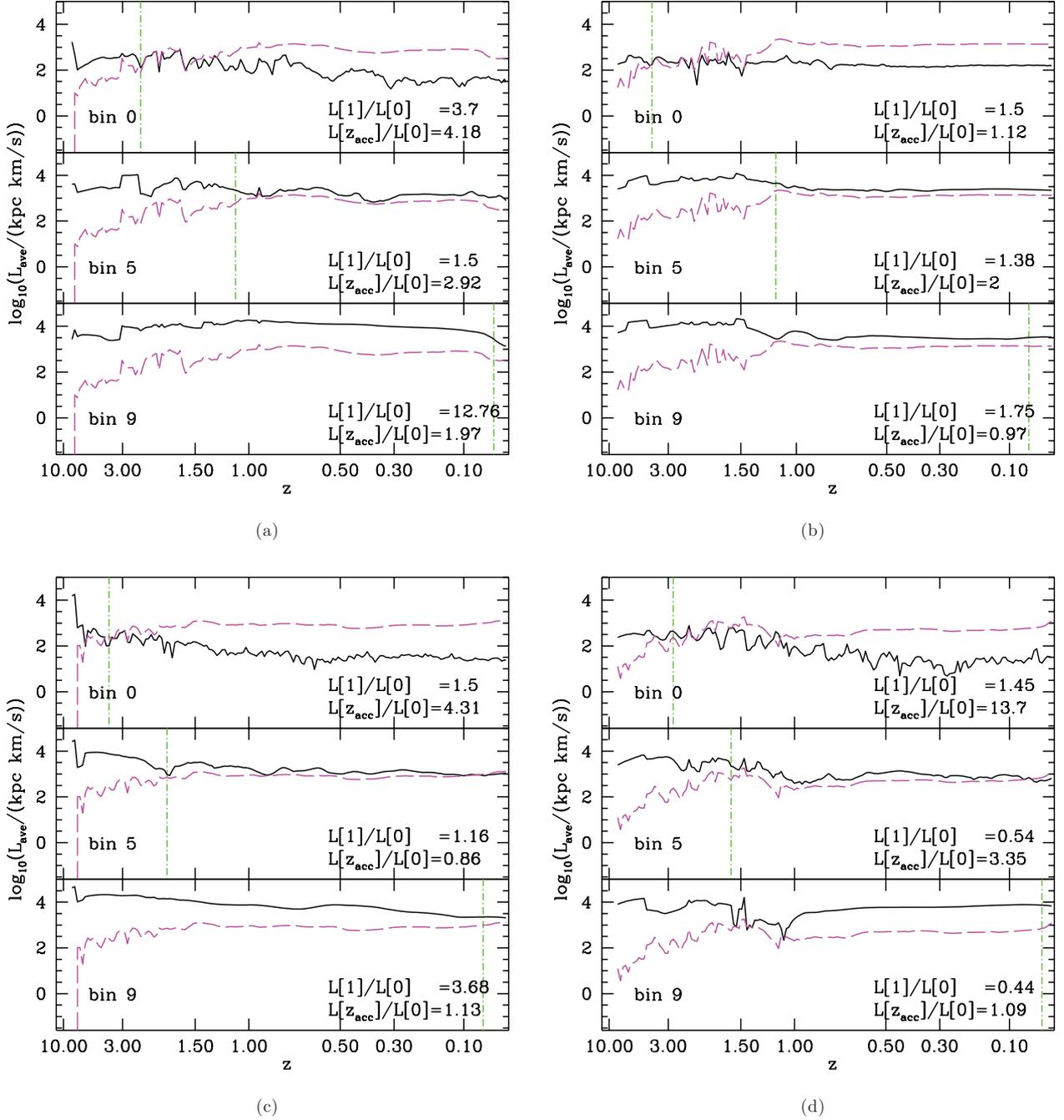
Figure 5. Similar to Fig. 4, except that the particles here are binned radially in a Eulerian fashion. The magenta long-dashed line shows the specific angular momentum of all halo particles within the virial radius at the given redshift.

We also examined the evolution of the angular momentum in radial shells when averaged using the magnitudes of particle angular momenta rather than vector-averaging. We have omitted plots of the magnitude-averaged cases as they are similar to Figs 4 and 5 and have instead included the relevant information about their evolution in Table 2. As we noted in Section 2.1, magnitude-averaged angular momenta tell us about the evolution of particle orbits, thus providing complementary information to the vector-averaged angular momenta that tell us about the evolution of the spin of radial shells. Further, it is the magnitude of angular momentum which is most relevant for the DF and adiabatic invariance.

The magnitude-averaged angular momenta evolve much more smoothly than the vector-averaged ones, indicating that cancellation

between particles in the vector-averaged case causes more variability than in the magnitude-averaged case. We show in Table 2 the values of $L[1]/L[0]$ and $L[z_{acc}]/L[0]$ for these cases. The particles that end up in the inner regions tend to have a higher angular momentum to start with than those particles that are in the innermost bin at the beginning of the simulation, and subsequently tend to lose this angular momentum more rapidly, though the effect is not as pronounced as in Fig. 4. The more pronounced nature of this effect in Fig. 4 indicates that the inner particles also tend to have their directions scrambled (i.e. are more thoroughly virialized) more than those in outer regions.

The mean magnitude-averaged angular momentum in each radial bin also decreases from the time of accretion to the present, while

Table 2. Ratios of the average binned angular momentum at $z = 1$ and at accretion of the radial bin to the value of the bin's average angular momentum at $z = 0$ for both Lagrangian- and Eulerian-selected radial bins, differing from Figs 4 and 5 in that the angular momenta are magnitude-averaged rather than vector-averaged.

| | Lagrangian | | | | | | Eulerian | | | | | |
| | Bin 0 | | Bin 5 | | Bin 9 | | Bin 0 | | Bin 5 | | Bin 9 | |
	L_1/L_0	L_{acc}/L_0	L_1/L_0	L_{acc}/L_0	L_1/L_0	L_{acc}/L_0	L_1/L_0	L_{acc}/L_0	L_1/L_0	L_{acc}/L_0	L_1/L_0	L_{acc}/L_0
H239	2.24	3.45	1.44	1.27	1.41	1.07	1.29	1.22	1.2	1.2	2.52	1.05
H258	2.42	5.96	1.21	1.23	1.3	1.03	1.31	1.31	1.08	1.29	1.81	0.99
H277	1.63	3.31	1.31	1.45	1.38	1.06	1.18	1.64	1.19	1.08	1.68	1.01
H285	1.22	3.55	1.11	1.1	1.05	0.99	0.95	1.36	1.04	1.12	1.28	1.02

the vector-averaged angular momenta in Fig. 5 in general decrease more since their accretion and have lower values. In both cases, the inner regions lose a larger fraction of their angular momentum than the outer regions. It should be noted that the trend of inner particles losing more angular momentum than outer particles was also found by Zavala et al. (2008). The generally larger decrease over time in the vector-averaged angular momenta implies that the scrambling, or decoherence, of angular momentum direction in the halo tends to increase over time.

Thus, we have found that those particles that end up in the inner regions of haloes lose a larger fraction of their angular momentum than other halo particles and that all of the particles in the halo tend to have the direction of their angular momenta scrambled progressively more over time. Further, we see that those particles that end up in the inner regions of the halo at $z = 0$ tend to start out with a higher angular momentum than those particles that are in the innermost bin at each time-step, and that they tend to lose this angular momentum more quickly.

3.3 Distribution of angular momentum

Next, we consider changes to the distribution of the magnitudes of the particle angular momenta, not just the average as shown in the last section. In Fig. 6, we show the distributions of angular momenta of all halo particles and inner halo particles for all four haloes. The top panels shows the angular momentum distribution of all particles within the virial radius chosen in a Eulerian fashion. Here, the number of particles, as well as their mean angular momentum, increases with time. In the middle and bottom panels, we show the evolution of 'inner' halo particles chosen in a Eulerian fashion, defined as those particles within $0.1\,r_{vir}(z = 0)$ (middle) and the innermost 90 000 particles corresponding to the innermost $10^{11}\,M_\odot$ (bottom). We also show in these panels the Boltzmann parametric fit $N = A\,\{\log_{10}[L/(kpc\,km\,s^{-1})] - \log_{10}(L_0)\}^2\{-[\log_{10}(L/(kpc\,km\,s^{-1})) - \log_{10}(L_0)]^2/2a^2\}$. The number of particles in the middle panels increases with time, while in the bottom panels it remains constant.

The inner particles have a lower average angular momentum than all halo particles, as is to be expected. The evolution of the distribution of angular momenta of all halo particles is qualitatively similar in all four haloes, with the average angular momentum of halo particles increasing with time as higher angular momentum particles are accreted.

Looking at the middle and bottom panels, we can see that for halo 277 the angular momentum distribution stays roughly constant in the inner regions, with few extra particles entering $0.1\,r_{vir}$ at each time-step. There is, however, a gradual decline in average angular momentum with time. This smooth evolution is related to the relatively quiescent evolution of halo 277. By contrast, we find

that the innermost $10^{11}\,M_\odot$ of halo 258 have a significantly lower average angular momentum after $z = 1$ than before, reflecting a major merger around this redshift. In general, all of these angular momentum profiles have a similar shape, which we find is fitted well by the above fitting function.

In all the haloes, though, there are changes of the angular momentum distribution with redshift. This implies that the angular momentum of a particle is strictly not an adiabatic invariant (or, perhaps, the time-scale for changes is not sufficiently slow for the adiabatic approximation to hold). This means that assuming that the DF is constant when expressed in terms of the angular momentum during periods when a galaxy is growing is formally incorrect. In practice, this lack of precise conservation simply sets a limit on how accurate the AC approach can ever be.

As a test, we show the fit parameters to the Boltzmann distribution as a function of redshift. In Fig. 7 we show the evolution of the parameters of the Boltzmann fitting function $N = A\{\log_{10}[L/(kpc\,km\,s^{-1})] - \log_{10}(L_0)\}^2 \exp\{-[\log_{10}(L/(kpc\,km\,s^{-1})) - \log_{10}(L_0)]^2/2a^2\}$, as shown in Fig. 6, for each of the four haloes we consider. The solid lines correspond to the particles selected to lie within $0.1r_{vir}(z = 0)$ in a Eulerian fashion, as in the middle panels of Fig. 6, while the dotted lines correspond to the innermost $10^{11}\,M_\odot$ as shown in the bottom panels of Fig. 6. The x-axis shows the redshift. Note that the discrete nature of the curves is a by-product of the discrete sampling of fit parameters used to determine the minimum χ^2 fit. The trends in these plots are qualitatively related to the merger history of the haloes. We know that halo 277 (c) is quite quiescent since around $z = 2$, which is reflected in the mostly smooth evolution of its fit parameters. Halo 258 (b), whose last major merger occurred around $z = 1$, shows roughly smooth evolution after this point. Haloes 239 and 285 (a and d), which have more active merger histories up to the present time, have more variation in their parameter evolution. As yet, though, we do not have a quantitative description of the fit parameters as a function of halo-evolution properties nor do we know if a quantitative fit is possible. Investigations into such a description would likely require a far larger statistical study than we have presented here.

4 CAUSES OF ANGULAR MOMENTUM EVOLUTION

We have seen that there is significant evolution over the history of these haloes of the average angular momentum (Section 3.2) and of the angular momentum distribution (Section 3.3). We now investigate the origin of the torques that are causing this non-conservation of angular momentum. There are several possibilities for the origin of these torques, including external structure, non-sphericity of the halo itself or infalling substructures, that we would expect to play
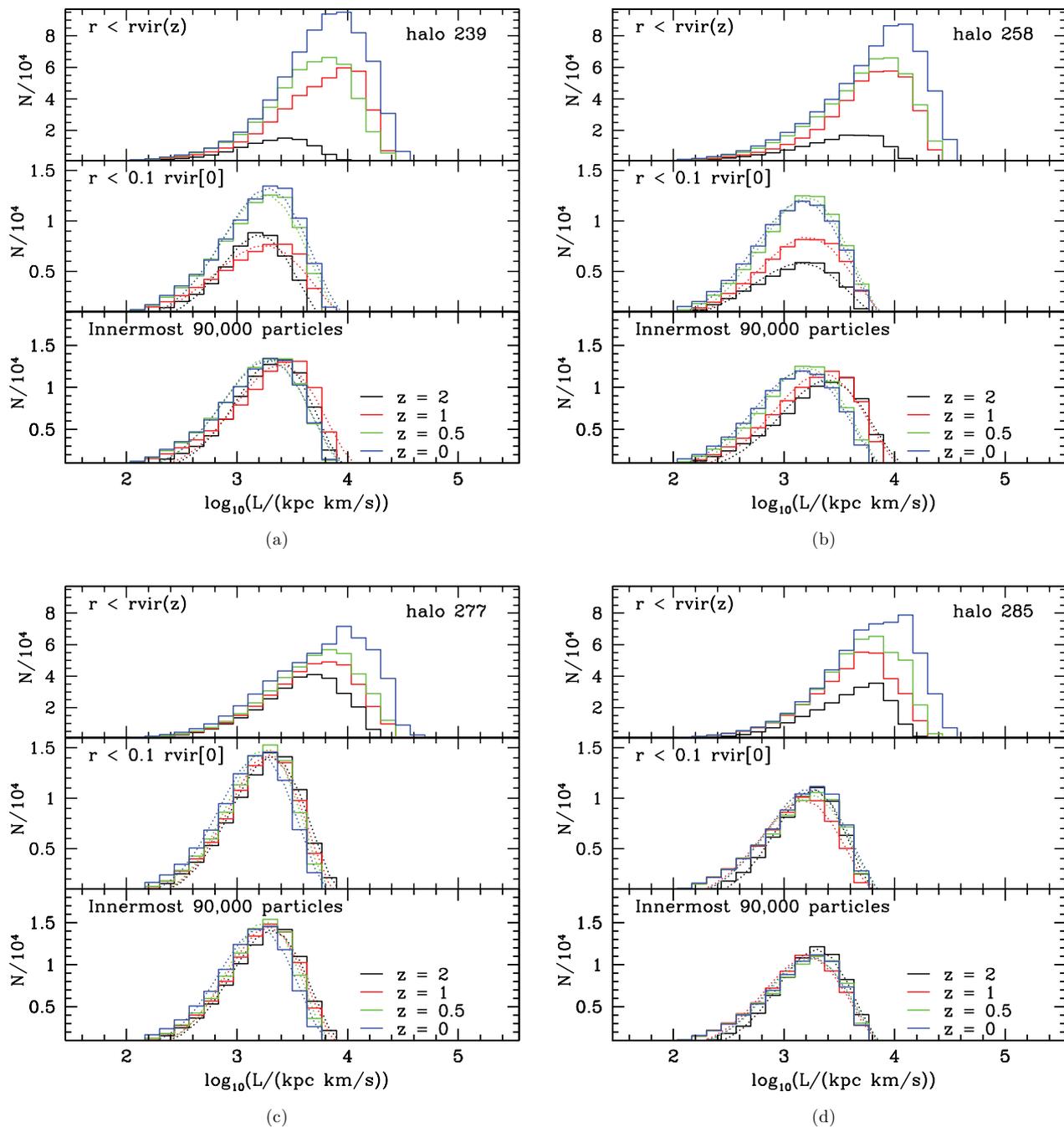
Figure 6. The evolution of the angular momentum of halo dark-matter particles for haloes (a) 239, (b) 258, (c) 277 and (d) 285. In each figure, the top panel shows the angular-momentum distribution of all particles within the virial radius selected in a Eulerian fashion. In the middle and bottom panels, we present the evolution of 'inner' halo particles, also selected in a Eulerian fashion, chosen radially (middle) and by mass (bottom). We also show in these panels the fit $N = A \{\log_{10}[L/(\mathrm{kpc\,km\,s^{-1}})] - \log_{10}(L_0)\}^2 \exp\{-[\log_{10}(L/(\mathrm{kpc\,km\,s^{-1}})) - \log_{10}(L_0)]^2/2a^2\}$ as dotted lines.

a role since we saw in the previous section that merger events are correlated with changes in the distribution of angular momenta.

To investigate the relative importance of these mechanisms to the inner halo, we show in Fig. 8 the time-scale associated with torques on the inner halo due to particles that are members of the host halo at $z = 0$ (blue dotted lines) and due to particles which are members of clumped substructures which will be within the virial radius at $z = 0$ (red dashed lines). We define the inner halo as those particles within the Eulerian-selected region $r(z) < 0.1r_{\mathrm{vir}}(z = 0)$. We compare this with the time-scale for the angular momentum to

change due to all torques, defined as the ratio of the total angular momentum of the inner region to its time derivative $L_{\mathrm{in}}/[\mathrm{d}L_{\mathrm{in}}/\mathrm{d}t]$ (black solid lines) and the inner halo dynamical time (magenta dot–dashed lines). Note that a longer time-scale here implies a weaker torque and conversely a small time-scale implies a strong torque that can change the angular momentum relatively quickly.

From these figures we can see that, in general, the time-scale for the angular momentum to change by order unity due to all external and internal torques is at least an order of magnitude less than that for the angular momentum to change due to torques only by

(a)   (b)   (c)   (d)
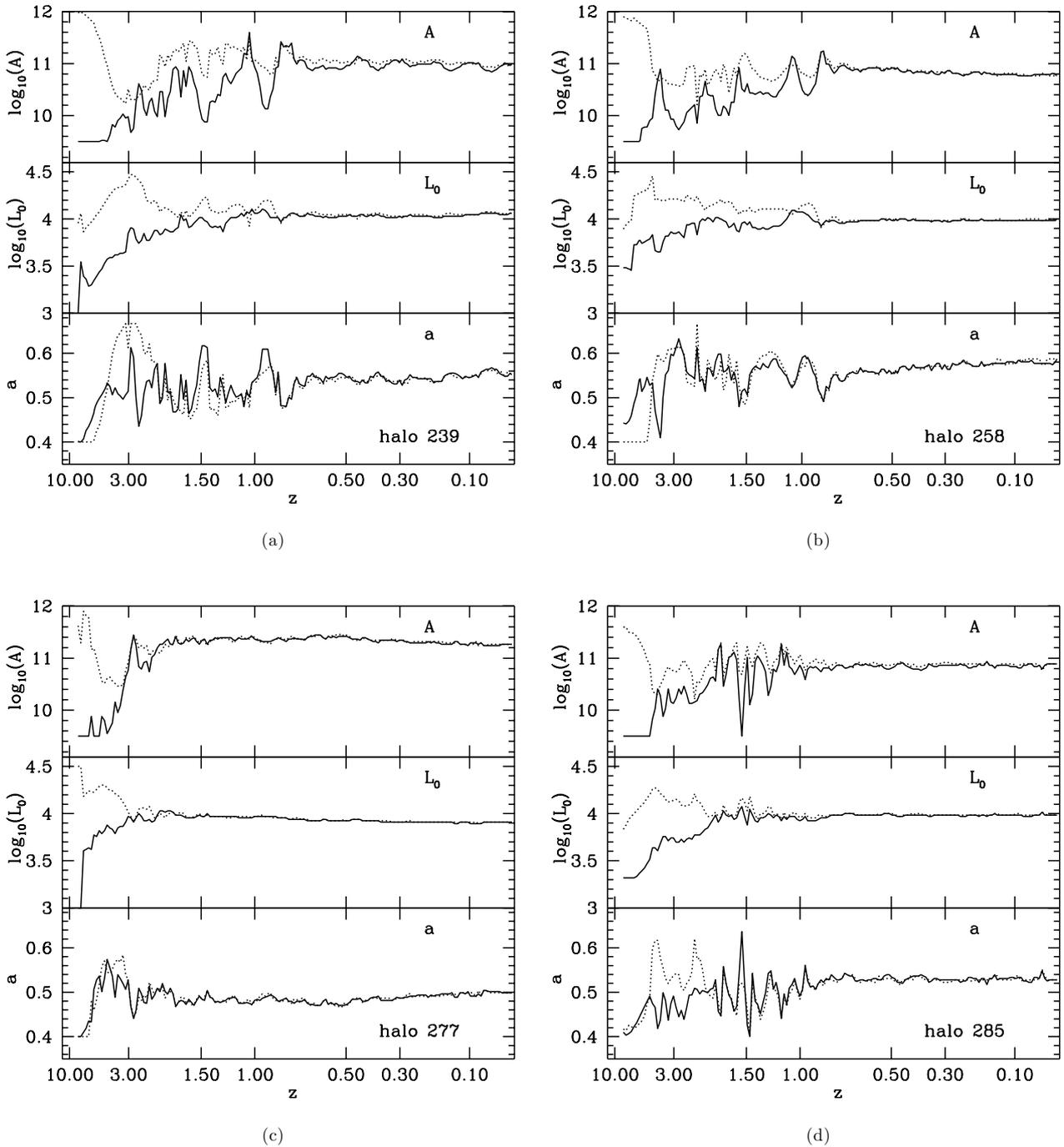
Figure 7. Evolution of the parameters of $N = A \{\log_{10}[L/(\text{kpc km s}^{-1})] - \log_{10}(L_0)\}^2 \exp\{-[\log_{10}(L/(\text{kpc km s}^{-1})) - \log_{10}(L_0)]^2/2a^2\}$, the Boltzmann fitting function in Fig. 6, shown here for each of the four haloes, where solid lines correspond to the particles selected to lie within $0.1r_{\text{vir}}(z = 0)$ as in the middle panels of Fig. 6, while the dotted lines correspond to the innermost $10^{11} \, M_\odot$ as shown in the bottom panels of Fig. 6. The x-axis shows the redshift. The trends in these plots are qualitatively related to the merger history of the haloes.

other particles in the halo or by clumped substructures, implying that the torques due to non-sphericity of the host halo and clumpy substructure are far weaker than torques due to external structure in the angular momentum evolution of the inner halo. Thus, external torques are the dominant source of angular momentum evolution of the inner halo as a whole. We also observe that all of these time-scales become large relative to the inner halo dynamical time during quiescent merger phases, for example after redshift $z \sim 1$ for halo 258, while the angular momentum change time-scale becomes

comparable to the dynamical time during mergers, both major and minor. This is reasonable, as it implies that the angular momentum changes slowly during periods of quiescent evolution. Note that the angular momentum change time-scale of halo 277 is closer to the dynamical time-scale during its quiescent evolution after $z = 3$, while the angular momentum change time-scale of halo 258 becomes significantly larger than its dynamical time-scale when it is quiescent after $z \sim 1$. This indicates that the speed of the evolution of angular momentum during quiescent phases does vary
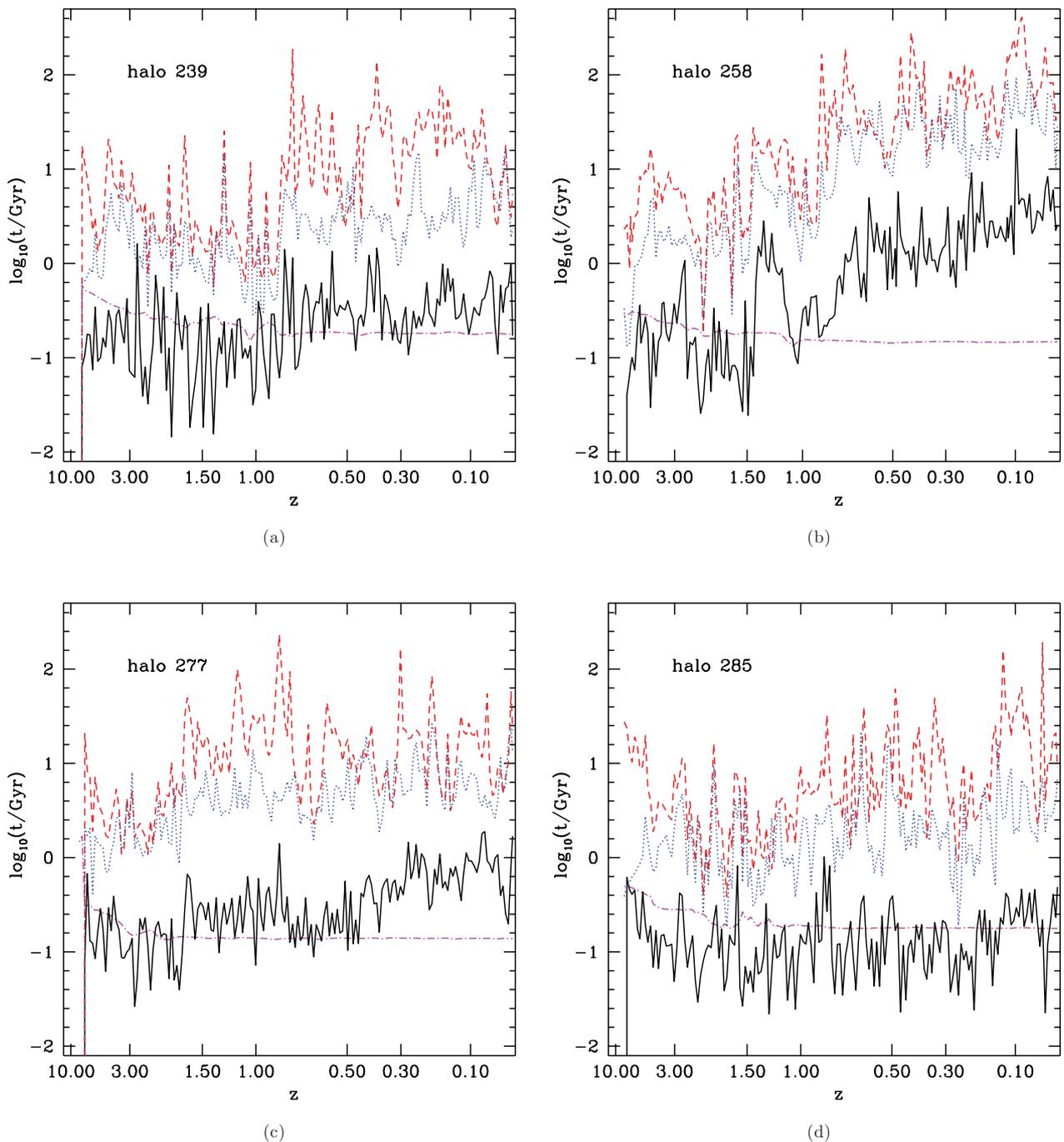
Figure 8. Time-scales associated with torques on the inner halo due to outer halo particles (blue dotted lines), clumpy substructure particles (red dashed lines) and all torques (black solid lines), for haloes (a) 239, (b) 258, (c) 277 and (d) 285. Also plotted is the inner halo dynamical time (magenta dot–dashed lines).

between haloes, probably due to the environment of the halo which is producing external torques.

We address the role played by these torques on individual particles in Fig. 9, in which we show the total torque dL/dt on selected particles (black solid lines) and compare this with the torque on these particles due to particles that are currently bound to the main halo and no other substructure (blue dotted lines) and particles which are members of clumped substructures at the given redshift that will be within the virial radius of the halo at $z = 0$ (red dashed lines). These torques are shown on a linear scale in the top panels, and their absolute value on a log scale is shown in the middle panels

of each figure. The difference between the sum of the torques due to halo particles and clumped particles and the total torque is the torque due to external structure, from particles that are not members of the halo at $z = 0$. The units of the torque in the top two panels are km kpc s^{-1} Gyr^{-1}. In the bottom panels, we show the radius of each individual particle (black solid lines) and compare it with the virial radius of the halo (green long-dashed lines) and the line $0.10r_{vir}(z = 0)$ (magenta dot–dashed lines) below which particles are classified as inner halo particles. The top three plots show three particles in halo 239, while the bottom three are from halo 258. For each halo we have randomly chosen one particle that spends most
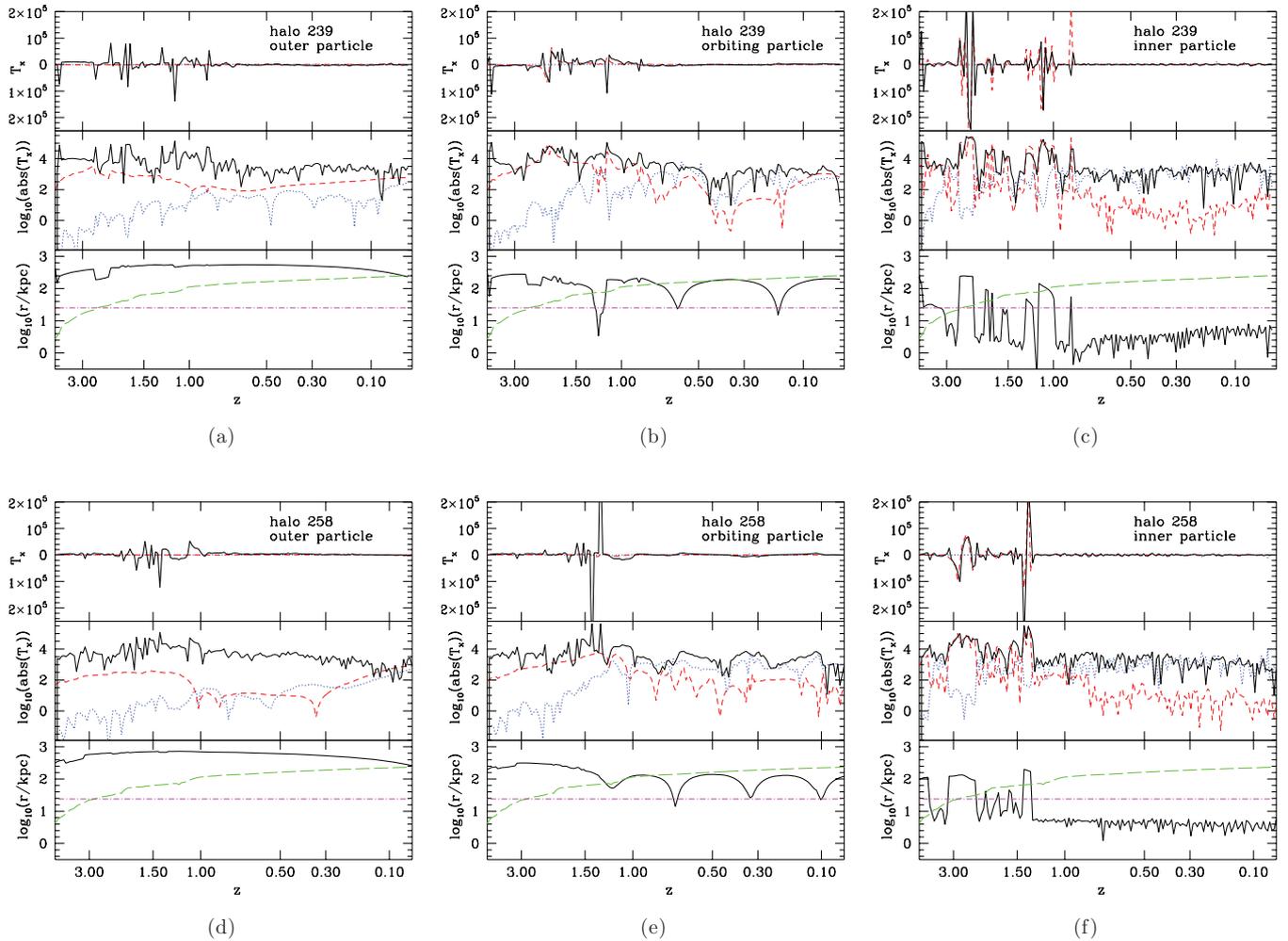
Figure 9. Total torque on selected halo particles (black solid lines) compared with the torque due to halo particles (blue dotted lines) and particles which are members of clumped substructures that will be within the virial radius of the halo at $z = 0$ (red dashed lines). The torque is shown on a linear scale in the top panel and its absolute value is shown on a log scale in the middle panel of each figure. The units of the torque in the top two panels are km kpc s^{-1} Gyr^{-1}. In the bottom panels, we show the radius of this particle (black solid lines) and compare it with the virial radius of the halo (green long-dashed lines) and the line $0.10r_{\rm vir}(z = 0)$ (magenta dot–dashed lines). The top three plots show three particles in halo 239, while the bottom three are from halo 258. For each halo, we have chosen one 'outer', one 'orbiting' and one 'inner' particle to show here.

of its time outside the virial radius ('outer particle'), one that orbits the halo, entering the virial radius on its closest approach ('orbiting particle'), and a particle that spends much of its time in the inner regions of the halo ('inner particle').

In general, we see that the torque on the individual particles that we have chosen is dominated by smaller subhaloes before the particle is accreted, but that this torque falls below that due to halo particles after the particle is accreted on to the halo. However, in Fig. 8 we saw that the angular momentum of the inner halo as a whole is dominated by external torques, with mergers also tending to lower the inner halo angular momentum. When taking the individual particle behaviour shown in Fig. 9 together with the behaviour of the entire inner halo in Fig. 8, we see that the importance of torques due to halo and clumped particles in the evolution of some of the individual particles goes away when considering the inner halo as a whole. Also, external structure, which plays a relatively minor role in the evolution of some of the individual particle angular momenta, is a dominant effect on the evolution of the total angular momentum of the inner halo. We may interpret this to say that external structure tends to torque each particle in the entire halo coherently, while

torques due to other halo particles and clumpy substructures can be larger on individual particles but are incoherent when considering the entire inner halo. If this is the case, then the torques due to halo particles will tend to cancel out when averaged over many individual particles in the inner halo, explaining the relative unimportance of these torques for the entire inner halo and why external structure comes to dominate the evolution of the inner halo.

5 DISCUSSION

We have analysed whether the assumptions of the AC model are valid in the case of simulated dark-matter haloes. Specifically, we have looked into whether such haloes can be characterized as adiabatically evolving and whether their angular momentum or angular momentum distributions are conserved as we would expect from the assumption of spherical symmetry in the model of AC most commonly applied to dark-matter haloes. We have found that the assumption of adiabatic evolution of haloes is not completely correct, that the angular momentum of regions of the halo is not an adiabatic invariant as is assumed in the AC model and that its

distribution also varies. We have investigated the sources of these torques and found that external torques are the main source of torque on the halo as a whole.

In greater detail, our major results are as follows.

(i) Halo particles follow the trend of centre-of-mass angular momentum expected from tidal torque theory.

(ii) In general, the gravitational potential of our haloes changes on time-scales larger than the dynamical time in the haloes, which is a prerequisite for adiabatic invariance. For the halo as a whole, the potential change time-scale is generally around an order of magnitude larger than the dynamical time-scale, while for the inner halo the potential change time-scale is only a factor of a few larger than the dynamical time-scale.

(iii) Angular momentum is lost from all particles as haloes virialize, more from those particles that end up in the centre of haloes. We find that both the vector- and magnitude-averaged angular momentum in fixed radial bins about the halo centre decreases with time, by a few tens of per cent to factors of a few. The vector-averaged quantities usually decrease more than the magnitude-averaged ones, implying that the directions of angular momenta in radial bins become progressively more misaligned over time.

(iv) The distribution of angular momentum magnitudes is well fitted by a simple Boltzmann fitting function. Trends in the evolution of these distributions qualitatively reflect the merger history of the halo.

(v) External torques dominate the angular momentum evolution of the inner halo, while substructure and halo non-sphericity torques can be important for the angular momentum evolution of individual particles. The dominant role of external torques in changing the angular momentum of halo particles agrees with the results of Valluri et al. (2010), who found the evolution of haloes during baryonic condensation to be mostly reversible when external torques were not included.

We find that halo particles are losing angular momentum even in these dark-matter-only simulations and that the net angular momentum loss of the inner regions of the halo is due mainly to external tidal torques. The amount of this decrease depends on what region we choose and how we add the angular momenta, but the ratio of angular momenta at $z = 1$ and $z = 0$ can vary from a few tenths to a few. The distribution of angular momenta in both the haloes as a whole and in the innermost parts in which a galaxy would live is not time-invariant, which means that the spherically symmetric form of AC that is typically applied to dark-matter halo profiles is not strictly valid.

While we find indications that the evolution in the angular-momentum distribution is correlated with the halo accretion histories, we have not found a quantitative description of these changes. Larger statistical studies are required to determine if a quantitative relation between the angular momentum distribution and halo accretion history can be established.

Many previous studies of AC have found it to overpredict the effect of baryon condensation on dark-matter density in the centres of haloes under the assumption that angular momentum is conserved. Our finding that angular momentum is lost from all particles in the halo over time likely exacerbates this problem, as it implies that even more mass would be concentrated in the centre due to dark-matter-only interactions. The interaction of the angular momentum loss of dark-matter particles observed here with baryonic physics is an interesting direction for future research.

The fact that angular momentum does not behave as a perfect adiabatic invariant is not surprising since, for example, haloes are non-spherical and evolve with time. Our results serve to highlight the magnitude of this issue and serve as a caution to applications of the AC approximation – there is a limit to the precision which we can reasonably expect it to provide. The fact that recent simulations show that no single model of AC works well in all cases (e.g. Gustafsson et al. 2006) suggests that this limit may have been reached. Overall, our results imply a fundamental limit to the applicability of current AC models which should be kept in mind when applying these approximations to the effects of galaxy formation on dark-matter haloes.

REFERENCES

Abadi M. G., Navarro J. F., Fardal M., Babul A., Steinmetz M., 2009, MNRAS, 407, 435
Abazajian K., Fuller G. M., Patel M., 2001, Phys. Rev. D, 64, 023501
Benson A. J., Bower R., 2010, MNRAS, 405, 1573
Benson A. J., Kamionkowski M., Hassani S. H., 2005, MNRAS, 357, 847
Binney J., Tremaine S., 2008, Galactic Dynamics, 2nd edn. Princeton Univ. Press, Princeton, NJ
Blumenthal G. R., Faber S. M., Flores R., Primack J. R., 1986, ApJ, 301, 27
Boylan-Kolchin M., Springel V., White S. D. M., Jenkins A., Lemson G., 2009, MNRAS, 398, 1150
Brooks A. M., Governato F., Quinn T., Brook C. B., Wadsley J., 2009, ApJ, 694, 396
Bullock J. S., Dekel A., Kolatt T. S., Kravtsov A. V., Klypin A. A., Porciani C., Primack J. R., 2001, ApJ, 555, 240
Cole S., Lacey C. G., Baugh C. M., Frenk C. S., 2000, MNRAS, 319, 168
Croton D. J. et al., 2006, MNRAS, 365, 11
de Blok W. J. G., Walter F., Brinks E., Trachternach C., Oh S.-H., Kennicutt R. C., 2008, AJ, 136, 2648
De Lucia G., Kauffmann G., White S. D. M., 2004, MNRAS, 349, 1101
Dubinski J., Carlberg R. G., 1991, ApJ, 378, 496
Duffy A. R., Schaye J., Kay S. T., Vecchia C. D., Battye R. A., Booth C. M., 2010, MNRAS, 405, 2161
Dutton A. A., van den Bosch F. C., 2009, MNRAS, 396, 141
Dutton A. A., van den Bosch F. C., Dekel A., Courteau S., 2007, ApJ, 654, 27
Eke V. R., Cole S., Frenk C. S., 1996, MNRAS, 282, 263
Feng J. L., Rajaraman A., Takayama F., 2003, Phys. Rev. Lett., 91, 011302
Gavazzi R., Treu T., Rhodes J. D., Koopmans L. V. E., Bolton A. S., Burles S., Massey R. J., Moustakas L. A., 2007, ApJ, 667, 176
Gill S. P. D., Knebe A., Gibson B. K., 2004, MNRAS, 351, 399
Gnedin O. Y., Kravtsov A. V., Klypin A. A., Nagai D., 2004, ApJ, 616, 16
Governato F., Willman B., Mayer L., Brooks A., Stinson G., Valenzuela O., Wadsley J., Quinn T., 2007, MNRAS, 374, 1479
Governato F. et al., 2009, MNRAS, 398, 312
Governato F. et al., 2010, Nat, 463, 203
Gross M. A. K., 1997, PhD thesis, Univ. of California
Gustafsson M., Fairbairn M., Sommer-Larsen J., 2006, Phys. Rev. D, 74, 123522
Hatton S., Devriendt J. E. G., Ninin S., Bouchet F. R., Guiderdoni B., Vibert D., 2003, MNRAS, 343, 75
Kaplinghat M., 2005, Phys. Rev. D, 72, 063510
Katz N., White S. D. M., 1993, ApJ, 412, 455
Klypin A., Trujillo-Gomez S., Primack J., 2010, preprint (arXiv:1002.3660)
Knollmann S. R., Knebe A., 2009, ApJS, 182, 608

Kuhlen M., Diemand J., Madau P., Zemp M., 2008, J. Phys. Conf. Ser., 125, 012008

Kuzio de Naray R., McGaugh S. S., de Blok W. J. G., 2008, ApJ, 676, 920

Mo H. J., Mao S., White S. D. M., 1998, MNRAS, 295, 319

Monaco P., Fontanot F., Taffoni G., 2007, MNRAS, 375, 1189

Navarro J. F., Frenk C. S., White S. D. M., 1997, ApJ, 490, 493

Navarro J. F. et al., 2004, MNRAS, 349, 1039

Navarro J. F. et al., 2010, MNRAS, 402, 21

Neistein E., Dekel A., 2008, MNRAS, 383, 615

Newman A. B., Treu T., Ellis R. S., Sand D. J., Richard J., Marshall P. J., Capak P., Miyazaki S., 2009, ApJ, 706, 1078

Padmanabhan N. et al., 2004, New Astron., 9, 329

Parkinson H., Cole S., Helly J., 2008, MNRAS, 383, 557

Peter A. H. G., Moody C. E., Kamionkowski M., 2010, Phys. Rev. D, 81, 103501

Pontzen A. et al., 2010, MNRAS, 402, 1523

Press W. H., Schechter P., 1974, ApJ, 187, 425

Read J. I., Mayer L., Brooks A. M., Governato F., Lake G., 2009, MNRAS, 397, 44

Reed D., Gardner J., Quinn T., Stadel J., Fardal M., Lake G., Governato F., 2003, MNRAS, 346, 565

Romano-Díaz E., Shlosman I., Heller C., Hoffman Y., 2008, ApJ, 687, L13

Romano-Díaz E., Shlosman I., Heller C., Hoffman Y., 2009, ApJ, 702, 1250

Schulz A. E., Mandelbaum R., Padmanabhan N., 2010, MNRAS, 408, 1463

Sheth R. K., Tormen G., 2002, MNRAS, 329, 61

Simon J. D., Bolatto A. D., Leroy A., Blitz L., Gates E. L., 2005, ApJ, 621, 757

Somerville R. S., Hopkins P. F., Cox T. J., Robertson B. E., Hernquist L., 2008, MNRAS, 391, 481

Spergel D. N., Steinhardt P. J., 2000, Phys. Rev. Lett., 84, 3760

Spergel D. N. et al., 2007, ApJS, 170, 377

Springel V. et al., 2005, Nat, 435, 629

Stadel J. G., 2001, PhD thesis, Univ. of Washington

Stadel J., Potter D., Moore B., Diemand J., Madau P., Zemp M., Kuhlen M., Quilis V., 2009, MNRAS, 398, L21

Tissera P. B., White S. D. M., Pedrosa S., Scannapieco C., 2010, MNRAS, 406, 922

Treu T., Koopmans L. V. E., 2004, ApJ, 611, 739

Tully R. B., Fisher J. R., 1977, A&A, 54, 661

Valluri M., Debattista V. P., Quinn T., Moore B., 2010, MNRAS, 403, 525

van den Bosch F. C., Burkert A., Swaters R. A., 2001, MNRAS, 326, 1205

van den Bosch F. C., Abel T., Croft R. A. C., Hernquist L., White S. D. M., 2002, ApJ, 576, 21

van den Bosch F. C., Abel T., Hernquist L., 2003, MNRAS, 346, 177

White S. D. M., 1984, ApJ, 286, 38

Zavala J., Okamoto T., Frenk C. S., 2008, MNRAS, 387, 364

Zhang J., Fakhouri O., Ma C., 2008, MNRAS, 389, 1521

Zolotov A., Willman B., Brooks A. M., Governato F., Brook C. B., Hogg D. W., Quinn T., Stinson G., 2009, ApJ, 702, 1058

This paper has been typeset from a TEX/LATEX file prepared by the author.